Documenting carved stones from 3D models. Part II - Ambient occlusion to reveal carved parts.

Tanguy Rolland, Fabrice Monna, Jérôme Magail, Yuri Esin, Nicolas Navarro, Josef Wilczek, Jamiyan-Ombo Gantulga, Carmela Chateau-Smith

Version of Record: https://www.sciencedirect.com/science/article/pii/S1296207421000571
Manuscript_3c632abc58d59c89142a0241c4d1aa7d

Documenting carved stones from 3D models. Part II - ambient occlusion to reveal carved parts

Tanguy Rolland[1,*], Fabrice Monna[1], Jérôme Magail[2], Yuri Esin[3], Nicolas Navarro[4,5], Josef Wilczek[1,6] , Jamiyan-Ombo Gantulga[7], Carmela Chateau-Smith[8]

[1]ARTEHIS, UMR CNRS 6298, Université Bourgogne–Franche Comté, 6 Boulevard Gabriel, Bat. Gabriel, 21000 Dijon, France

[2]Musée d'Anthropologie préhistorique de Monaco, 56 bis, boulevard du Jardin exotique, 98000 MC, Monaco

[3]Khakassian Research Institute for Language, Literature and History, 23, Shchetinkin Street, 655017 Abakan, Republic of Khakassia, Russia

[4]EPHE, PSL Research University, 21000 Dijon, France

[5]Biogéosciences UMR CNRS 6282, Université Bourgogne Franche-Comté, 6, boulevard Gabriel, 21000 Dijon, France

[6]Department of Archaeology, University of Hradec Králové, Rokitanského 62, 50003 Hradec Králové, Czech Republic (present address).

[7]Institute of Archaeology, Mongolian Academy of Sciences, Jucov street-77, Ulaanbaatar-13343, Mongolia

[8]CPTC, EA4178, Université de Bourgogne, 4, boulevard Gabriel, 21000 Dijon, France

Length of the manuscript: 5621 words

Keywords: Archaeology, deer stone, rock art, Late Bronze Age, Mongolia, documentation, volumetric obscurance

*: tanguy.rolland@u-bourgogne.fr, tel: +33 (0) 3 80 39 57 97

Abstract: Revealing carved parts in rock art is of primary importance and remains a major challenge for archaeological documentation. Computational geometry applied to 3D imaging provides a unique opportunity to document rock art. This study evaluates five algorithms and derivatives used to compute ambient occlusion and sky visibility on 3D models of Mongolian stelae, also known as deer stones. By contrast with the previous companion work, models are processed directly in 3D, without preliminary projection. Volumetric obscurance gives the best results for the identification of carved figures. The effects of model resolution and parameters specific to ambient occlusion are then evaluated. Keeping tridimensional information intact allows accurate measurement of distance, volume, and depth. Objects augmented by ambient occlusion can easily be manipulated in 3D viewers, for seamless and effortless access to the overall organization of the figures, at the scale of the entire object. Qualitatively speaking, the 2D projected outputs are equivalent to, or even better than, existing archaeological documentation. The proposed workflow should be easily applicable in many situations, particularly as the functions provided for the free R programming software are fully configurable.

1. Introduction

In recent years, several authors have applied 3D modeling techniques to the documentation of rock art [1-6], benefiting from advances in computational power, and field operability, particularly when using photogrammetry [3,7-9]. Beyond the excellent correspondence between model geometry and the real-word artefact, two notable advantages of 3D capture over traditional methods (*i.e.* rubbing and tracing) are (*i*) the absence of potentially damaging contact with the object to be acquired, and (*ii*) the speed of the process, as time is a major limiting factor in the field. With textured 3D models, it is also possible to simulate, in virtual scenes, different lightning conditions, including grazing light. This long-standing photographical technique, together with reflectance transformation imaging (RTI), can be used by archaeologists to darken carved areas [10,11]. Recent approaches have considered geometry, when it is essentially planar, as a topographical surface to which geospatial methods can be applied. In this case, the geometry of the model is represented as a raster image, where pixel values correspond to altitude, producing a digital elevation model (DEM). Relief may be perceived using computed-generated lighting: analytical hill-shading, for example [12]. For essentially planar surfaces (e.g. engraved walls or slabs), an optimized trend removal procedure (e.g. local relief model, LRM) can also be used to delineate carvings [6]. The recent companion work proposed a practical workflow for dealing with less specific flat surfaces, such as roughly parallelipipedic objects [13]. The study focused on the famous Mongolian deer stones dating from the Late Bronze Age. These stelae, up to 4 m high, often made of granite or sandstone, are engraved with numerous decametric figures (animals, weapons, ornaments, etc.) on each side. After obtaining 3D meshes by photogrammetry, a 2.5D raster DEM was produced by planar projection on each of the four vertical sides of the stela, to capture the entire set of figures. Projecting on the four sides of the stela was natural here, because it corresponds to the traditional representation of such parallelipipedic objects in archaeological documentation. Several algorithms based on differential geometry, sky visibility (sky-view factor [14-16] and positive openness [17,18]), and local morphology were then evaluated. Positive openness was identified as one of the most efficient algorithms for highlighting carved parts and surface

condition of stelae. However, rock art is not only found on simple flat geometrical surfaces, such as parallelepipeds. It may also be found on irregular, curved, or concave surfaces, and even on volumetric solids. In such cases, the approaches enumerated above may be difficult to apply, and may strongly deform any symbols depicted in the final results. It would therefore be advantageous to process the entire 3D model in order to overcome these limitations, and not be limited to a subset of cases consisting mostly of roughly flat surfaces, such as those discussed in previous studies [1,10]. Incorporating the results directly into the 3D models, depicted over a color scale, would be an undeniable asset for further examination and better understanding of the carved object. One practical solution is ambient occlusion (AO), introduced at the end of the twentieth century [19-21], and developed since then by the video game industry [22-24]. The aim is to obtain a photorealistic rendering, with minimum computational cost, by simulating shadows in darkened concave and occluded parts of a scene, and by highlighting open areas. Ambient occlusion may be approximated in different ways, but is similar in approach to sky visibility methods, which were specifically designed for DEMs.

Research aims. The purpose of this study is to test several approaches previously developed to compute ambient occlusion (also including sky-view factor and positive openness computations adapted for entire 3D models) and, if possible, to propose guidelines for enhancing carved areas. Scripts were produced with a single programming platform, R, and are made freely available for a broad archaeological audience. The effect of several extrinsic (model resolution) and intrinsic parameters (specific to AO algorithms) are evaluated. The results are then compared to existing archaeological documentation, and to results previously published in the companion study for two deer stones in a good state of conservation, but with different surface conditions: well-marked carving and slightly marked carving.

2. Material & methods

2.1. Corpus

Deer stones, belonging to funeral structures built by nomads in the late 2nd – early 1st millennium BC, are widespread in Mongolia. More than 1200 deer stones have been identified, and classified into three groups [26, 27]. The stelae studied here all belong to the same group, found mostly in Central and East Mongolia. They are decorated with numerous carved figures (both centimetric and decametric), among which deer are the most emblematic, with mature antlers, elongated heads, long necks, and legs folded under their bellies. Other subjects are represented, including several kinds of weapons, shields, belts, and necklaces, forming a well-structured composition. The vast number of visual elements on this type of deer stone makes them the most time-consuming to document. Two previously documented stelae (#35 and #36; in [13]), located in the Bayantsagaan valley of Khoid Tamir, are used here to evaluate the algorithms, and then compare results with those from the companion study. Eleven stelae, located at the Jargalantyn am complex site, Khanui River valley, Arkhangai, were also processed. All the 3D meshes were obtained by photogrammetry during the Monaco-Mongolian joint mission, undertaken in 2015. The entire acquisition workflow using Structure-from-Motion is detailed in the companion study [13]. Briefly, about thirty to a hundred pictures were captured at a distance varying from 2 to 5 m, with cameras placed approximately 1 meter apart, depending on the size of the stelae. Pictures were treated with PhotoScan (https://www.agisoft.com/), and the resulting 3D model was scaled using a self-retracting metallic measuring tape, placed at the foot of the stela and incorporated into the pictures. Two different cameras were used: a hand-held NIKON D800 semi-pro fullframe DSLR (sensor 24 × 36 mm, 36 Mpix), equipped with NIKKOR 24 mm or 50 mm prime lenses (for stelae #35 and #36); a consumer grade compact SONY DSC-RX100 MIII (sensor 13.2 × 8.8 mm, 20 Mpix), 24–70 mm in 24 × 36 equivalent, was used with the focal set at 24 mm (for Jargalant stelae). With this setup, the ground pixel size can be estimated at between 0.2 mm and 0.5 mm. The planar accuracy is between 0.06 mm and 0.15 mm, and the depth accuracy between 0.12 mm and 0.75 mm [28]. Textured 3D models are

in Polygon File Format (PLY) format, with a typical resolution of 1-3 mm (i.e. mean edge length between vertices) for 3D models with 3-12 M vertices.

2.2. The algorithms tested

2.2.1. Principle of ambient occlusion

Shadows play an important role in the perception of the world, as they provide information about the position of objects relative to each other, and their surface condition [20]. In virtual worlds, they result from direct or ambient illumination and are essential for realistic rendering. Ambient occlusion represents the amount of ambient light reaching a point in a 3D scene, so that points receiving little light are darkened. Real-time calculation capabilities using the "*screen-space*" approach appeared in 2007 [21,29]. The 3D scene is projected on to a 2D space and AO is calculated only on the visible parts. Distances between points and their projection in the image space are represented as a depth map (or depth buffer). The idea underlying screen-space is quite similar to the approach proposed in the companion study, where the four DEMs could be considered as four depth maps, and where the algorithms based on visible sky (i.e. sky view factor and positive openness) followed the same philosophy as AO. Here, the idea is rather to calculate AO using the "object-space" approach; in other words, by considering all points of the 3D scene, and not only those visible from the observer's point of view. Note that AO is not obtained by formal calculation, but by Monte Carlo approximation, applied to limited zones surrounding each vertex of the 3D model. The algorithms listed below were suited to our purpose: darkening the carved, concave areas of the deer stones, and highlighting the convex areas.

2.2.2. Ambient occlusion inspired by the Crytek approach

This process was originally developed in 2007 by Crytek, a video game company, for a game named Crysis. Each point, *P*, of the 3D model becomes the centre of a sphere of radius *r*, in which *n* sample

points, s_i with i ∈ [1;n], were randomly placed (Fig. 1a). Then AO was defined as the ratio between the number of samples visible from *P*, and the total number of samples:

$$AO = \frac{1}{n} \times \sum_{i=1}^{n} V(s_i) \quad \text{eq. 1,}$$

with $V(s_i)$ = 1 if s_i was visible from *P*, and 0 otherwise. Some authors have suggested adapting this method using only one hemisphere instead of the complete sphere [30]. In this study, the hemisphere was positioned by making its zenith coincide with either (*i*) the normal vector of *P*, $\vec{n}_P$, (Fig. 1b), or (*ii*) the normal of a 3D best-fit regression plane (BFRP) of vertices with the radius *r*, $\vec{n}_{BFRP}$ (Fig. 1c). In all three cases, AO was obtained by eq. 1. and values ∈ [0;1].

2.2.3. Ambient occlusion deriving from sky-view factor and positive openness

These two methods, commonly used in spatial analysis [14-18] to treat DEMs, have been adapted to process 3D models. In both cases, the purpose is to determine the portion of visible sky limited by the relief. Here, the Sky-view factor adapted for 3D models, namely 3D-SVF, takes into account one hemisphere (orientated either with $\vec{n}_{BFRP}$ - cf. Fig. 1d -, or with $\vec{n}_P$, not shown), decomposed into *k* (commonly 8) radial portions. The altitude angles, θ_k, from which the sky becomes visible, are then computed, and hence the 3D-SVF, ranging between 0 and 1, is calculated similarly to the normal SVF following:

$$3D - SVF = 1 - \frac{\sum_{i=1}^{k} \sin(\theta_k)}{k} \quad \text{eq. 2.}$$

Positive openness, PO, is also defined by eight radial directions. For each of them, the greatest angle ϕ_k, relative to the zenith (and not to the horizon) was computed (Fig. 1e). For 3D models, 3D-PO values correspond to the average of these angles [18], after making the zenith coincide with $\vec{n}_P$:

$$3D - PO = \frac{\Phi 0 + \Phi 45 + \cdots + \Phi 315}{8} \quad \text{eq. 3,}$$

so that 3D-PO ∈ $[0;\pi]$. Programmatically, *j* samples were placed evenly along the celestial meridian for 3D-SVF (or terrestrial meridian for 3D-PO), for each radial direction.

2.2.4. Volumetric obscurance-based method, VO

This AO is defined as the ratio between the volume inside the model and the volume outside the model of a given sphere centred at point *P* [31]. A line sampling strategy is used to approximate these two volumes. A total of *n* sample points was first placed randomly on a disc of radius *r*, centred on *P*, and parallel to the BFRP. The lines sampled in this study were those between each sample point and its projection on to the surface of both hemispheres following the normal direction of the disc (Fig. 1f). Finally, VO was defined as the ratio between the total lengths of the segments outside the model, $Lout_i$, and those inside, Lin_i; $VO \in]0;+\infty[$:

$$VO = \frac{\sum_{i=1}^{n} Lout_i}{\sum_{i=1}^{n} Lin_i} \qquad \text{eq. 4.}$$

2.2.5 Global illumination, GI

In its simplest form, AO can be obtained from global illumination. In practice, lighting is simulated from *n* light sources, l_i, scattered on the surface of a sphere with a radius much greater than that of the object size (Fig. 1g). The GI was defined by the rate of illumination that a vertex received:

$$GI = \frac{1}{n} \times \sum_{i=1}^{n} W(l_i) \quad \text{eq. 5,}$$

with $W(l_i)$ =1, if the vertex *P* received the light l_i, and 0 otherwise.

2.3 Numerical comparison of the enhancement capabilities of each algorithm

A subset of the model for stela #35 was retained for formal comparison of the enhancement capabilities of the six methods. The carved parts were represented by manually selected vertices corresponding to the limits of the carvings, comprised between the top and the foot of the slope. The remaining vertices correspond to uncarved parts (see Supplementary Material S1). Two variables were considered: (i) the ambient occlusion (AO) computed by each method, as described above, and (ii) the spatial variability of the AO, using the inverse distance weighting variance as a proxy, calculated within a radius r (the same measurement was used for AO computation). The 1D-

Wasserstein distance, W_1, which measures the area between two cumulative distribution functions, was used as the metric to evaluate the differences between carved and uncarved parts, following [32-34]:

$$W_1 = \int_{x=-\infty}^{+\infty} |F(x) - G(x)| dx \quad \text{eq. 6,}$$

where F(x) and G(x) are the cumulative distribution functions to be compared. In practice, all tested variables were first standardized to eliminate the scale factor. A higher value for the Wasserstein distance (W_1) indicates greater difference between carved and uncarved parts, based on their distributions for each variable, thus leading to easier recognition of the engravings.

2.4. Programming implementation

Scripts for producing AO were written using the free R software (https://www.r-project.org/), with the help of the functions included in the `Rvcg` [35], `rgl` [36], `Morpho` [37], `cwhmisc` [38], `HI` [39] and `doParallel` [40] packages. Briefly, the position or visibility of sample points in relation to the model is obtained by raytracing. To improve performance, partition by nearest neighbour search was operated by kd-tree. Additional details can be found in the script files provided as supplementary materials (see Supplementary Material S2). The proposed method should be easily applicable; the functions provided are configurable and adjustable to any acquisition workflow based on 3D modelling.

3. Results and discussion

3.1. Algorithm comparison

Most of the algorithms were tested with a sphere or hemisphere of 1 cm radius, a value previously found appropriate to enhance the figures carved on these particular stelae [13]. For the GI method,

1024 lights were distributed at 100 m from the object (i.e. a value much greater than the normal size of a deer stone of ca. 1- 4 m). When required (in the VO- and Crytek-approaches), a total of 200 points was sampled. Tests were carried out on unsmoothed models of stelae #35 and #36, decimated to 500 000 faces. The AO values obtained were then truncated at the 1st and 9th deciles, and converted into grey scale. This step greatly improves the overall contrast and facilitates visual comparisons between different renderings. Note that algorithms using hemisphere orientation with either the normal of P or of BRFP produced similar results (see Supplementary Material S3 for more detail), so that only the outputs using BRFP are presented in the following.

The symbols carved on the two largest sides of stela #35 are barely visible (Fig. 2a-b). The Crytek-based approaches computed using either the sphere (Fig. 2c-d) or the hemisphere (Fig. 2e-f) produce very different, but clearly sub-optimal outcomes. With the sphere, the carved parts were darkened, but they were not clearly distinguished from the surrounding area, which was also dark, and even noisy. With the hemisphere, the stela appeared mainly whitish, with almost only the footslopes of the deeply carved parts strongly darkened (Fig. 2e-f). The less pronounced depressions were barely visible, while information about the surface condition of the stone was lost. The 3D-SVF (also using the hemisphere, Fig. 2g-h) generally suffered from the same drawbacks, but a little more detail could be perceived, particularly in the shallow areas. Although 3D-PO (Fig. 2i-j) follows the same underlying idea as 3D-SVF, their respective outputs were quite different. With 3D-PO, the deer were fully marked, as were small irregularities on the surface of the stone that did not adversely affect the overall reading of the stela. This result is mainly due to the capacity of 3D-PO to account for convex parts, while 3D-SVF cannot distinguish planes from convex areas [14]. Such behavior was already observed on DEMs, and it is for this reason that PO was previously preferred to other methods, including SVF [13]. The VO-based approaches (Fig. 2k-l) produced similar results to those obtained with 3D-PO. The central part of the deer appeared darker, and less noisy, whereas the carved edges were much more strongly contrasted. Interestingly, in principle, VO is less prone to be affected by small surface irregularities close to the point of interest P, because calculations are based on volume,

and not on visibility, which can be drastically affected by any protruding neighbors blocking the view. The VO approach should therefore produce more readable results, even with stelae presenting rather granular surfaces. The general appearance with GI (Fig. 2m-n) was smoother than that obtained with all the other methods. Concave areas, whatever their dimensions, were clearly enhanced, as were the carved edges. Although results were acceptable on the essentially convex side (Fig. 2m), they were locally less so on the opposing, slightly concave side (Fig. 2n). The GI method appears to be very dependent on the overall shape of the object. However, even if GI seems to be unsuitable for complex 3D objects, it may be effective for flat carved surfaces (see Supplementary Material S4, for an example).

Computed Wasserstein distances for AO and AO spatial variability are reported in Fig. 3, and cumulative distribution functions are displayed in Supplementary Material S5. These results confirm the first observations by the naked eye. Among all tested methods, the VO algorithm produces the highest Wasserstein distances for both variables, especially for spatial variability. This is a clear sign of high local contrast and strong discontinuities in carved parts, which should make the figures more easily identifiable.

3.2. Optimal parameters

The influence of all parameters, both extrinsic (model resolution) and intrinsic (radius and sampling points), should be examined to optimize the VO algorithm for the delineation of carved figures. As computation time increases with each of these variables, the goal is to obtain relevant output (for our purpose) without computational overload.

3.2.1. Model resolution

The aim here was to assess the minimum model resolution at which carvings can be properly highlighted. The VO algorithm was applied to four models of stela #35, originally with ca. 3 M faces,

and progressively decimated to 2 M, 1 M, 500 k, and 250 k faces, thus producing resolutions of 1.99 mm, 2.80 mm, 3.96 mm, and 5.62 mm, for the average edge length (Fig. 4). The variance of the Laplacian was used as a metric for sharpness [41,42]. Its value increases from 367 to 738 (see Fig. 4), indicating slightly more detailed outputs as the number of faces grows, thus improving pattern contour accuracy. In all cases, the carvings always remain easily readable, whatever the model resolution tested. Surface states of the object are slightly better rendered with models possessing more faces. Here, one million faces is more than adequate to identify and study figures.

3.2.2. Influence of the radius *r*

The radius must be set according to the size of the details to be highlighted. It is well known that smaller *r* values tend to capture more noise, while higher *r* values essentially provide information about the overall shape of the object [25]. Three radii were tested: 0.5 cm, 1 cm, and 2 cm, on a model possessing 1 M faces (Fig. 5). The variance of the Laplacian was again used to analyze the outputs. The increase of the radius leads to a clear decrease in sharpness, with values falling from 657 to 302 (Fig. 5). At a radius of 0.5 cm, both patterns and surface irregularities were well marked. At 1 cm, only the smallest irregularities disappeared, while pattern boundaries remained clearly distinguishable from model roughness. At 2 cm, surface roughness was no longer rendered, and figure boundaries were somewhat blurred. As a result, a radius of 1 cm was a good compromise: figure edges were easily identifiable, and the information about surface condition was preserved, without being overly affected by potential noise.

3.2.3. Influence of number of sample points

Theoretically, with more samples, the estimation of the volume of interest should be more accurate. Three different setups for processing VO were tested: 10, 100, and 1000 samples. The reference considered here was 1000 samples. Between 100 and 10 samples, the mean absolute errors increase slightly from 0.011 ± 0.011 (1SD) to 0.027 ± 0.031 (1SD), meaning a deviation of only about 1-3% (see

Supplementary Material S6). Such deviations can be considered insignificant, providing no visual difference in terms of rendering (Fig. 6). In addition, no systematic bias could be identified for either of the two cases (see Supplementary Material S6). As a result, 10 samples should be enough to properly enhance the relief, while saving computation time. Such a finding is in agreement with the sampling parameters commonly used in ambient occlusion algorithms, i.e. 8-16 samples [21,31].

3.3. 2D projection and comparison with current documentation

At this point, it is worth recalling that, by contrast with the previous companion study, the figures are now enhanced directly on the 3D model itself, and not from a set of 2D projections. The operator can therefore manipulate the object in a dedicated viewer, to examine the relationships between the figures, and thus perceive their organization in a true 3D space. Measurements that were impossible (or at least difficult) in the 2D projected space are now achievable: e.g. volumes, Euclidian or geodesic distances, and depth (Fig. 7). Working from an enhanced 3D model also offers new and very flexible possibilities for projecting archaeological objects appropriately (more particularly for objects with irregular geometries) in order to produce accurate 2D documentation. To assess the effectiveness of the approach proposed in this study (Fig. 8), the results for the targeted side of stela #36 extracted from existing documentation, for orthomosaic (Fig. 8a), rubbing (Fig. 8b), and SAGA-based positive openness applied on a DEM (Fig. 8c) were compared with results obtained using the VO-based approach (Fig. 8d). Figure 8c is based on results in [13], which used the same 3D model as the present study, but limited the DEM to a resolution of 1 mm per pixel, judged sufficient to extract the geometry of the carved areas.

Shape and position of the figures are virtually identical for all techniques, except for orthomosaic, which is not informative. Although the deepest figures can be systematically identified (e.g. the circle at the top of the stela and all the deer), rendering appears much more contrasted with the VO-based approach (Fig. 8d), so that figures are generally better distinguished. The faintly carved bow and horse (Fig. 8e-f), barely visible with PO, are better distinguished with VO. Note, however, that

rubbing still provides the best outputs for these details. Neither the arrow and the top of the bow, nor the horse's ears and nose can be detected with VO. This drawback should not be formally imputed to the VO-based approach, but to the resolution of the original model, which was not detailed enough to record such discreet surface features. The bow, as well as the details of the horse, do in fact become discernable when a supplementary 3D model, produced at better resolution (0.4 mm), is used as input (Fig. 8e-f).

The method described can be applied routinely. As an example, eleven stelae from the Jargalantyn am complex site, processed by volumetric obscurance and projected on their four main sides can be found (see Supplementary Material S7), as well as the enhanced 3D models in PLY format (see Supplementary Material S8). A close examination of the upper part of the treated Jargalant N°2-2 stela, compared to the corresponding available documentation [43] (Fig. 9), plainly reveals the attractive potential of the approach presented here. In addition to circles well recorded by tracing (noted #1 in Fig. 9a-c), two new small circles are now clearly visible with the VO-based approach on the 3D model (noted #2 in Fig. 9a-c). The reason is probably their shallower depth of carving: roughly 2 mm for the new figures vs. 3-4 mm for the already recorded figures (Fig. 9c). Here, the large, deep circle with rays resembling both the sun and one of the types of earrings from the Late Bronze Age in the eastern steppes appears to overlap one of these small circles (arrow Fig. 9a,c), and the front part of the deer's antler (noted #3 in Fig. 9a), providing information about phasing in carved figures. During the first stage, the deer and the two previously unidentified circles must have been carved. Later, these circles must have been almost completely erased to incorporate the "sun" and another circle. This is supported by the fact that there are never two such small circles on the same side of deer stones. Rubbing succeeded better than tracing in identifying all figures covering this stela, and probably also in illustrating differences observed in carving depth. However, in contrast with rubbing, the interpretations drawn from VO are not only based on visual inspection of the outputs. A return to the original 3D model, containing the tridimensional geometry, is always possible for further measurements. Here, the acquisition process was not adapted to a techno-traceological study, but

the algorithms described could straightforwardly be applied to another model acquired specifically for this purpose.

4. Conclusion

Ambient occlusion, straightforwardly assessed by volumetric obscurance from 3D meshes, is a powerful tool to reveal carvings. Although the suggested configuration operates well in our case, it is recommended that researchers take advantage of the versatility of the proposed method by tuning the parameters for their specific purposes. The ability to routinely produce of a set of 3D models, textured by a choice of ambient occlusion algorithms, should help archaeologists to trace outlines of carved figures in a great variety of conditions. Grayscale rendering greatly facilitates the identification of carved images, which are underlined by strongly contrasted edges. Relief enhancement also provides information about the surface condition of the stone, at the time of acquisition. Keeping the tridimensional knowledge of the object intact throughout the whole process is an undoubted asset. One of the most significant advances concerns the extended handling capacity for rock art survey. As preliminary 2D projections are not necessary, information loss does not occur and complex reprojection of documentation is not required. Distance, volume, and depth can be accurately measured, and enhanced objects can easily be manipulated in 3D viewers, making it simpler to perceive the organization of (possibly overlapping) figures, which may be present on all sides. The operator is in full control, and can select whichever 2D projection best fits the objectives of the study. This flexibility is particularly appreciable for complex shapes. Note that the augmented version of the 3D models may advantageously incorporate virtual scenes for purposes of communication to a broader audience [44]. Although convex protruding areas, such as the edges of the stelae, may be partly bleached, which may somewhat mask carvings, the VO-based approach is nevertheless much more versatile than tracing or rubbing, which are difficult to apply to very

irregular objects. Although the conservation state of the carved areas on the objects and the quality of 3D modelling will obviously affect the quality of the outputs, the results obtained with the VO-based approach almost equal, and sometimes even surpass, existing archaeological documentation, while preventing possible degradation of the surface, and significantly reducing the time required on site for acquisition.

Acknowledgements

This research was funded by the Joint Mission Mongolia–Monaco and the project ROSAS (uB-FC and RNMSH).

References

[1] A. Simpson, P.Clogg, M. Díaz-Andreu, B. Larkman, 2004, *Towards three-dimensional non-invasive recording of incised rock art*, Antiquity*, 78*(301),p. 692-698, https://doi.org/10.1017/S0003598X00113328.

[2] M. Carrero-Pazos, A. Vázquez-Martínez, B. Vilas-Estévez, 2016, *AsTrend: Towards a new method for the study of ancient carvings*, Journal of Archaeological Science: Reports, 9, p. 105-119, https://doi.org/10.1016/j.jasrep.2016.06.044.

[3] J.L. Lerma, S. Navarro, A. Seguí, M. Cabrelles, 2014, *Range-Based Versus Automated Markerless Image-Based Techniques For Rock Art Documentation*, The Photogrammetric Record, 29, p.30-48, https://doi.org/10.1111/phor.12054.

[4] G. Plets, W. Gheyle, G. Verhoeven, J. De Reu, J. Bourgeois, J. Verhegge, B. Stichelbaut, 2012, *Three-dimensional recording of archaeological remains in the Altai Mountains*, Antiquity*, 86*(333), 884-897, https://doi.org/10.1017/S0003598X00047980.

[5] S. Cassen, V. Grimaud, 2017, Enregistrements, représentations et analyse structurale d'une stèle néolithique gravée dans l'ouest de la France. Kermaillard à Sarzeau (Morbihan, France), Bolletino del Centro camuno di Studi Preistorici, 43, p. 33-56.

[6] R. Hesse, 2010, *LiDAR-derived Local Relief Models – a new tool for archaeological prospection*, Archaeological Prospection, 17, p. 67 – 72, https://doi.org/10.1002/arp.374.

[7] A. Velios, J.P. Harrison, 2001*, Laser scanning and digital close range photogrammetry for capturing 3D archaeological objects : A comparison of quality and practicality*, In Archaeological Informatics : Pushing the Envelope CAA 2001, British Archaeological Reports International Series : Oxford, UK, Volume 1016, p. 567–574.

[8] M. Vavulin, I. Nevskaya and L. Tybykova, 2019, *DIGITAL MACRO-PHOTOGRAMMETRY IN DOCUMENTATION OF OLD TURKIC RUNIFORM INSCRIPTIONS IN THE ALTAI MOUNTAINS*, Mediterranean Archaeology and Archaeometry, Vol. 19, N° 2, p. 81-104.

[9] G. Plets, G. Verhoeven, D. Cheremisin, R. Plets, J. Bourgeois, B. Stichelbaut, W. Gheyle, J. De Reu, 2013, *The deteriorating preservation of the Altai Rock art : assessing three-dimensional image-based modelling in rock art research and management*, Rock art research, 29, p.139-156.

[10] M. Díaz-Guardamino, L. García Sanjuán, D. Wheatley, V. Rodríguez Zamora, 2015, RTI and the study of engraved rock art : A re-examination of the Iberian south-western stelae of Setefilla and Almadén de la Plata 2 (Seville, Spain), Digital Applications in Archaeology and Cultural Heritage 2, Elsevier, p. 41-54.

[11] G. Palma, M. Corsini, P. Cignoni, R. Scopigno, M. Mudge, 2010, *Dynamic shading enhancement for reflectance transfor-mation imaging*. ACM J. Comput. Cult. Herit. 3, 2, Article 6 (September 2010), 20p. DOI : 10.1145/1841317.1841321 http://doi.acm.org/10.1145/1841317.1841321.

[12] M. Carrero-Pazos, B. Vilas-Estévez, A. Vázquez Martínez, 2018, *Digital imaging techniques for recording and analysing prehistoric rock art panels in Galicia (NW Iberia)*, Digital Applications in Archaeology and Cultural Heritage, 8, p. 35-45, https://doi.org/10.1016/j.daach.2017.11.003.

[13] F. Monna et al., 2018, *Documenting carved stones by 3D modelling – Example of Mongolian deer stones,* Journal of Cultural Heritage*,* https://doi.org/10.1016/j.culher.2018.04.021.

[14] K. Zaksek, K. Ostir, Z. Kokalj, 2011, *Sky-View-Factor as a Relief Visualization Technique*, Remote Sensing, n°3, p. 398-415.
[15] J. Dozier, J. Frew, 1990, *Rapid calculation of terrain parameters for radiation modeling from digital elevation data*, IEEE Transact. Geosci, Remote Sens, 28, p. 963–969.

[16] T.E. Oke, 1987, *Boundary layer climates*, Routledge Ed, 464p.

[17] M. Doneus, 2013, *Openness as Visualization Technique for Interpretative Mapping of Airborne Lidar Derived Digital Terrain Models*, Remote Sensing, 5, p. 6427-6442, https://doi.org/10.3390/rs5126427.

[18] R. Yokoyama, M. Shirasawa, R. J. Pike, 2002, *Visualizing Topography by Openness: A New Application of Image Processing to Digital Elevation Models*, Photogrammetric Engineering & Remote Sensing, vol. 68, n°3, p. 257-265.

[19] G. Miller, 1994, *Efficient algorithms for local and global accessibility shading*, SIGGRAPH '94: Proceedings of the 21st annual conference on Computer graphics and interactive techniques, p. 319-326, https://doi.org/10.1145/192161.192244.

[20] M.S. Langer et S.W. Zucker, 1994, *Shape-from-shading on a cloudy day*, Journal of the Optical Society of America A, vol. 11, n°2, p. 467-478.

[21] M. Mittring, 2007, *Finding next gen: Cryengine 2 (course notes)*, In ACM SIGGRAPH 2007 courses, ACM, SIGGRAPH 2007, p. 97–121.

[22] J.Bokšanský, A.Pospíšil, J.Bittner, 2017,*VAO++: Practical Volumetric Ambient Occlusion for Games,* Eurographics Symposium on Rendering - Experimental Ideas & Implementations, The Eurographics Association, p. 31-39, https://doi.org/10.2312/sre.20171192.

[23] D. Holden, J. Saito, T. Komura, 2016, *Neural Network Ambient Occlusion*, S*IGGRAPH ASIA 2016 Technical Briefs*, ACM, 4p.

[24] M. McGuire, B. Osman, M. Bukowski, P. Hennessy, 2011, *The Alchemy Screen-Space Ambient Obscurance Algorithm*, HPG '11 Proceedings of the ACM SIGGRAPH Symposium on High Performance Graphics, ACM, p. 25-32.

[25] K. Vardis, G. Papaioannou, A. Gaitatzes, 2012, *Multi-view Ambient Occlusion with Importance Sampling*, I3D '13 Proceedings of the ACM SIGGRAPH Symposium on Interactive 3D Graphics and Games, ACM, p. 111-118.

[26] V.V. Volkov, Olennye kamni Mongolii, Nauchnyi mir, Moscow, 2002, pp. 248 (in Russian).

[27] Turbat T. (ed.). Mongol ba bus nutgiin bugan khushuunii soyol. Erdem shinzhilgeenii katalog, in 2 vol. ADMON, Ulaanbaatar, 2018 (in Mongolian).

[28] B. P.Hudzietz, S. Saripalli, 2011, *AN EXPERIMENTAL EVALUATION OF 3D TERRAIN MAPPING WITH AN AUTONOMOUS HELICOPTER*, International Archives of the Photogrammetry, Remote Sensing and Spatial Information Sciences, Volume XXXVIII-1/C22, p. 137-142.

[29] C. Dachsbacher, J. Kautz, 2009, *Real-Time Global Illumination for Dynamic Scenes Screen Space Techniques*, SIGGRAPH '09 ACM SIGGRAPH 2009 Courses, ACM, 33 p.

[30] D.Filion, R.McNaughton, 2008, *Effects & techniques.In ACM SIGGRAPH 2008 Games*, ACM, New York, NY, USA, SIGGRAPH ’08, p. 133–164.

[31] B. J. Loos, P.-P. Sloan, 2010, *Volumetric obscurance*, Proceedings of the 2010 ACM SIGGRAPH symposium on Interactive 3D Graphics and Games, ACM, p. 151–156.

[32] A. Ramdas, N. G. Trillos, M. Cuturi, 2017, *On Wasserstein Two-Sample Testing and Related Families of Nonparametric Tests*, Entropy, 19, 47, 15p., https://doi.org/10.3390/e19020047.

[33] G. Freitag, C. Czado, A. Munk, 2007, A nonparametric test for similarity of marginals—With applications to the assessment of population bioequivalence, Journal of Statistical Planning and Inference, 137, p. 697-711, https://doi.org/10.1016/j.jspi.2006.06.003.

[34] E. Del Barrio, J. Cuesta-Albertos, C. Matran, J. Rodriguez-Rodriguez, 1999, Tests of Goodness of Fit Based on the L2-Wasserstein Distance, The Annals of Statistics, Vol. 27, n°4, p. 1230-1239, http://www.jstor.org/stable/120161.

[35] S. Schlager, G. Francois, 2017, http://github.com/zarquon42b/Rvcg, 43p.

[36] D. Adler, D. Murdoch and others, 2018, https://r-forge.r-project.org/projects/rgl/, 153p.

[37] S. Schlager, G. Jefferis, D. Ian, 2018, https://github.com/zarquon42b/Morpho, 162p.

[38] C.W. Hoffman, 2018, http://www.echoffmann.ch, 91p.

[39] G. Petris, L. Tardella, 2013, https://cran.r-project.org/web/packages/HI/HI.pdf, 9p.

[40] R. Calaway, Microsoft Corporation, S. Weston, D. Tenenbaum, 2017, https://cran.rproject.org/web/packages/doParallel/doParallel.pdf, 4p.

[41] J. L. Pech Pacheco, G. Cristobal, J. Chamorro-Martinez, J. Fernandez-Valdivia, 2000, Diatom autofocusing in brightfield microscopy: A comparative study, Pattern Recognition, Proceedings, 15th International Conference on, 3, p. 314-317, https://doi.org/10.1109/ICPR.2000.903548.

[42] S. Pertuz, D. Puig, M. García, 2012, Analysis of focus measure operators in shape-from-focus, Pattern Recognition, 46, p. 1415–1432, https://doi.org/10.1016/j.patcog.2012.11.011.

[43] T. Turbat, J. Bayarsaikhan, D. Batsukh, N. Bayarkhuu, 2011, *DEER STONES of the JARGALANTYN AM*, Mongolian Tangible Heritage Association NGO, 192p.

[44] F. Monna, N. Navarro, J. Magail, R. Guillon, T. Rolland, J. Wilczek, Y. Esin, C. Chateau, *Contextualization of Archaeological Information Using Augmented Photospheres, Viewed with Head-Mounted Displays*, Sustainability 2019, 11, 3894, 13p., https://doi:10.3390/su11143894

Caption:

Fig. 1 Illustration of the approaches tested. (a) Crytek-based approach using spherical area sampling. (b) Crytek-based approach using hemispherical area sampling oriented by normal of P. (c) Crytek-based approach using hemispherical area sampling oriented by the BFRP. Blue points represent samples seen by P, and red points samples that are not seen. (d) 3D-Sky-view factor. (e) 3D-Positive openness. (f) Volumetric obscurance-based approach. Blue lines represent segment parts outside the mesh, and red lines parts inside the mesh. (g) Global illumination method with examples of ray tracing to determine whether samples on the surface can see points on the model.

Fig. 2 Comparison between the rendering of the tested methods applied to stela #35. (a-b) Orthomosaic. (c-d) Crytek-based approach using spherical area sampling. (e-f) Crytek-based approach using hemispherical area sampling. (g-h) 3D-Sky-view factor. (i-j) 3D-Positive openness. (k-l) Volumetric obscurance-based approach. (m-n) Global illumination.

Fig. 3 Wasserstein distances between carved and uncarved parts for a subset of stela #35. Data for AO in light blue, and spatial variability of AO in dark blue. Note that input data were first standardized. AO: ambient occlusion.

Fig. 4 Effect of model resolution, using stela #35 as an example, with the volumetric obscurance-based approach. Number of faces tested: 250000 (a), 500000 (b), 1M (c) and 2M (d). From top to bottom: projection of one side after processing the entire stela, a close-up corresponding to the red inset, the value of the variance of Laplacian computed from the projection.

Fig. 5 Effect of radius of influence, *r*, using stela #35 as an example, with the volumetric obscurance-based approach. The three radii tested are 0.5 cm (a), 1 cm (b), 2 cm (c). From top to bottom: projection of one side after processing the entire stela, a close-up corresponding to the red inset, the value of the variance of Laplacian computed from the projection.

Fig. 6 Effect of the number of sampling points, using stela #35 as an example, with the volumetric obscurance-based approach. Number of samples tested: 10 (a), 100 (b), 1000 (c).

Fig. 7 Example of measurement, using stela #35 as an example. Euclidian distance (green dotted line) and geodesic distance (red line) between points A and B.

Fig. 8 Comparison between the results of rubbing, positive openness, and the volumetric-based approach on two faces of stela #36. (a) Orthomosaic, (b) Rubbing, (c) Positive openness on DEMs, (d) Volumetric-based approach, (e) bow detail (yellow outline), (f) horse detail (purple outline). For both (e) and (f), from left to right: rubbing, archaeological drawing from rubbing, treatment by positive

openness of a DEM, see [13], volumetric-based approach with 3D models with a resolution of either 2.7 mm or 0.4 mm.

Fig. 9 Comparison between the results of tracing, rubbing and the volumetric-based approach on the top of two faces of Jargalant N°2-2 stela. (a) from left to right, results of tracing, rubbing and the volumetric-based approach. (b) from left to right, results of tracing and the volumetric-based approach. (c) Cross-section of stela faces with plots showing variations in relief. (1) in red: circles recorded by tracing. (2) in green: circles visible with the VO-based approach.

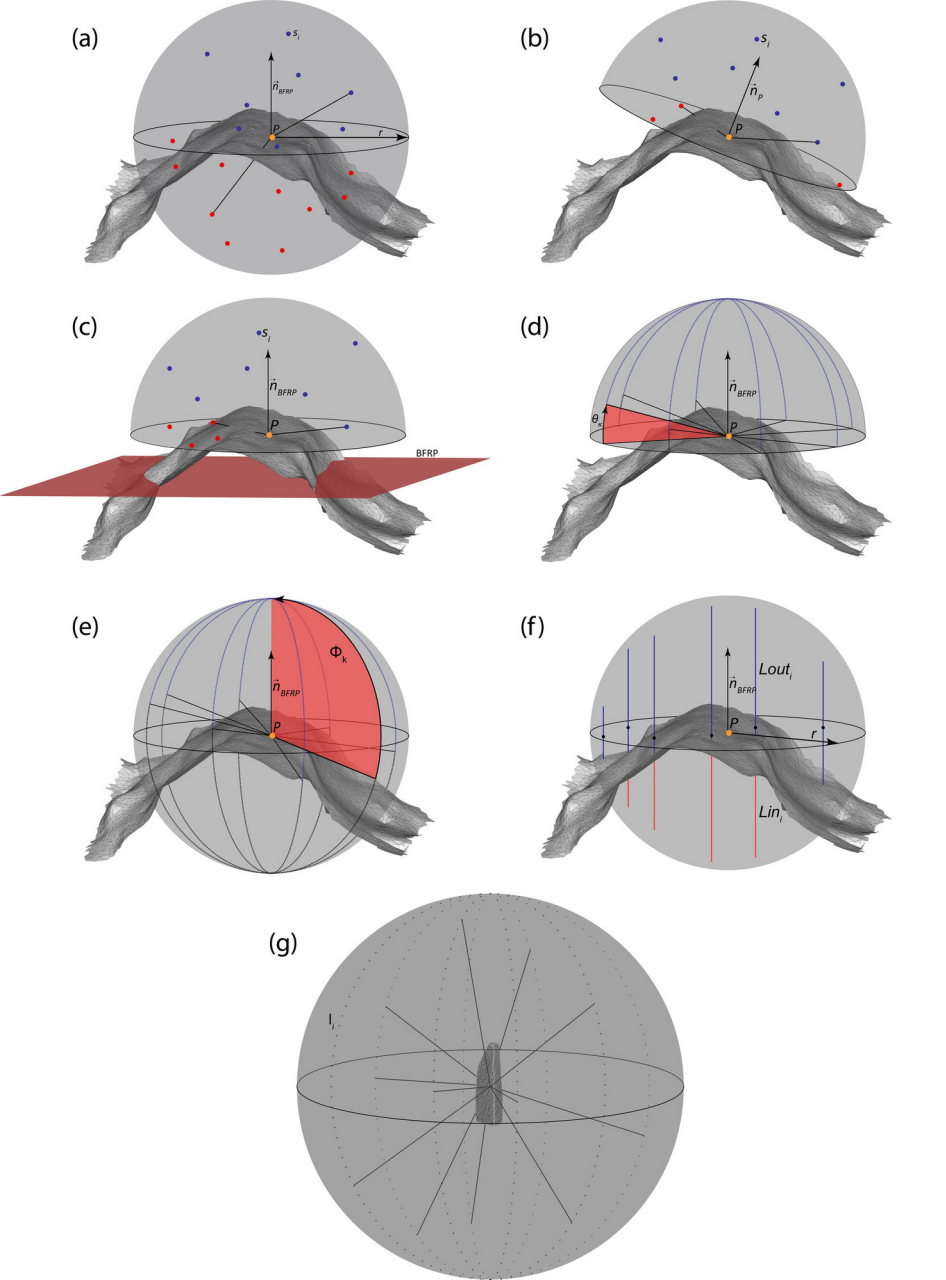
(a)
s_i
$\vec{n}_{BFRP}$
P
r
(b)
s_i
$\vec{n}_P$
P
(c)
s_i
$\vec{n}_{BFRP}$
P
BFRP
(d)
$\vec{n}_{BFRP}$
θ_k
P
(e)
Φ_k
$\vec{n}_{BFRP}$
P
(f)
$Lout_i$
$\vec{n}_{BFRP}$
P
r
Lin_i
(g)
I_i

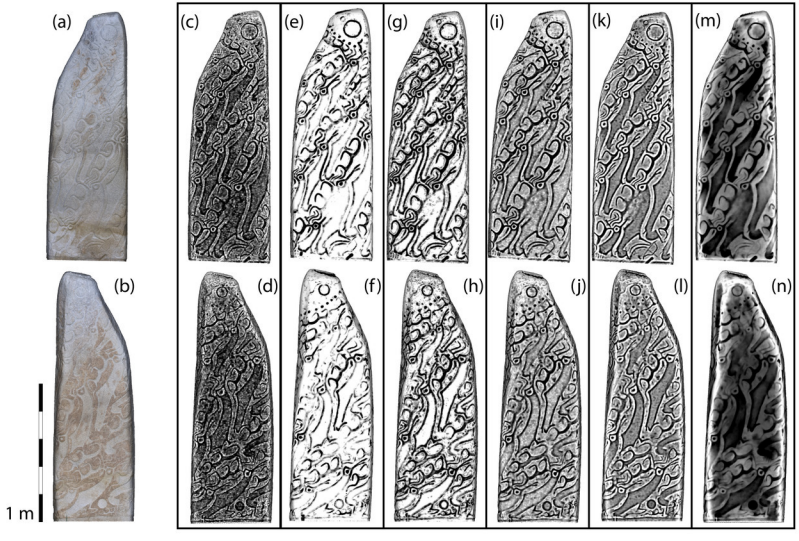
(a)
(b)
(c)
(d)
(e)
(f)
(g)
(h)
(i)
(j)
(k)
(l)
(m)
(n)
1 m

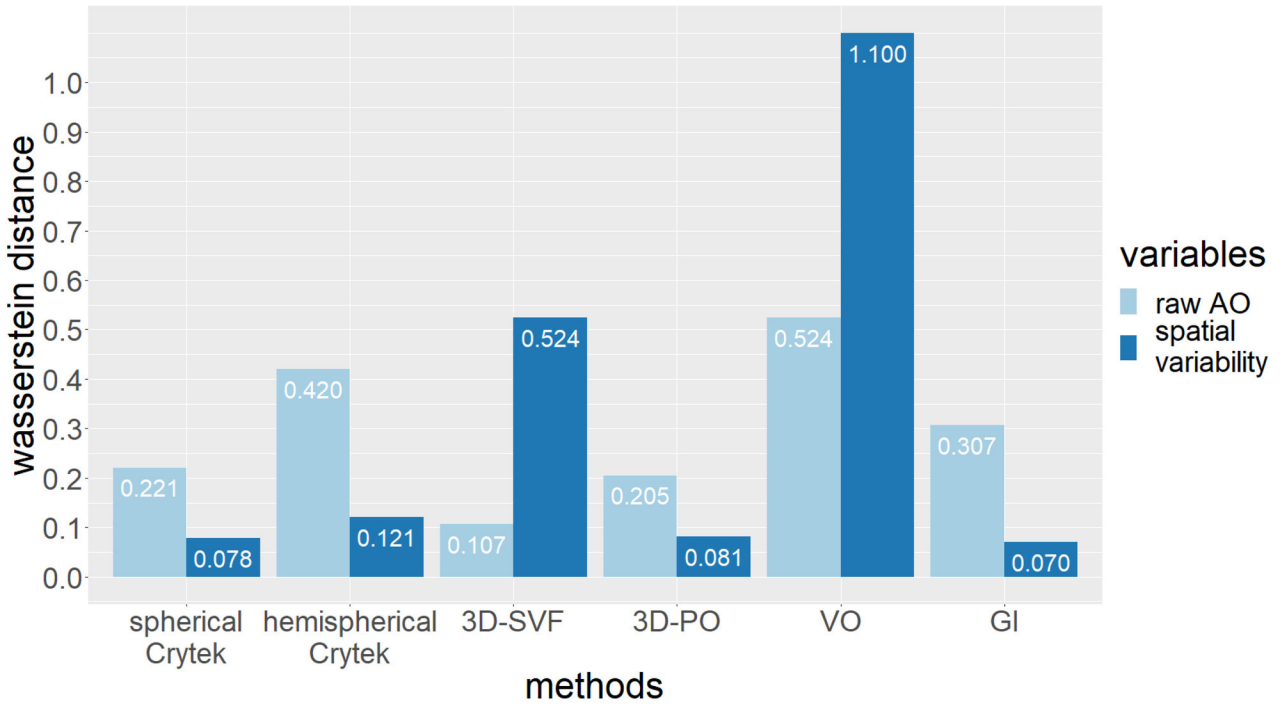
wasserstein distance
1.0
0.9
0.8
0.7
0.6
0.5
0.4
0.3
0.2
0.1
0.0
0.221
0.078
0.420
0.121
0.107
0.524
0.205
0.081
0.524
1.100
0.307
0.070
spherical Crytek
hemispherical Crytek
3D-SVF
3D-PO
VO
GI
methods
variables
raw AO
spatial variability

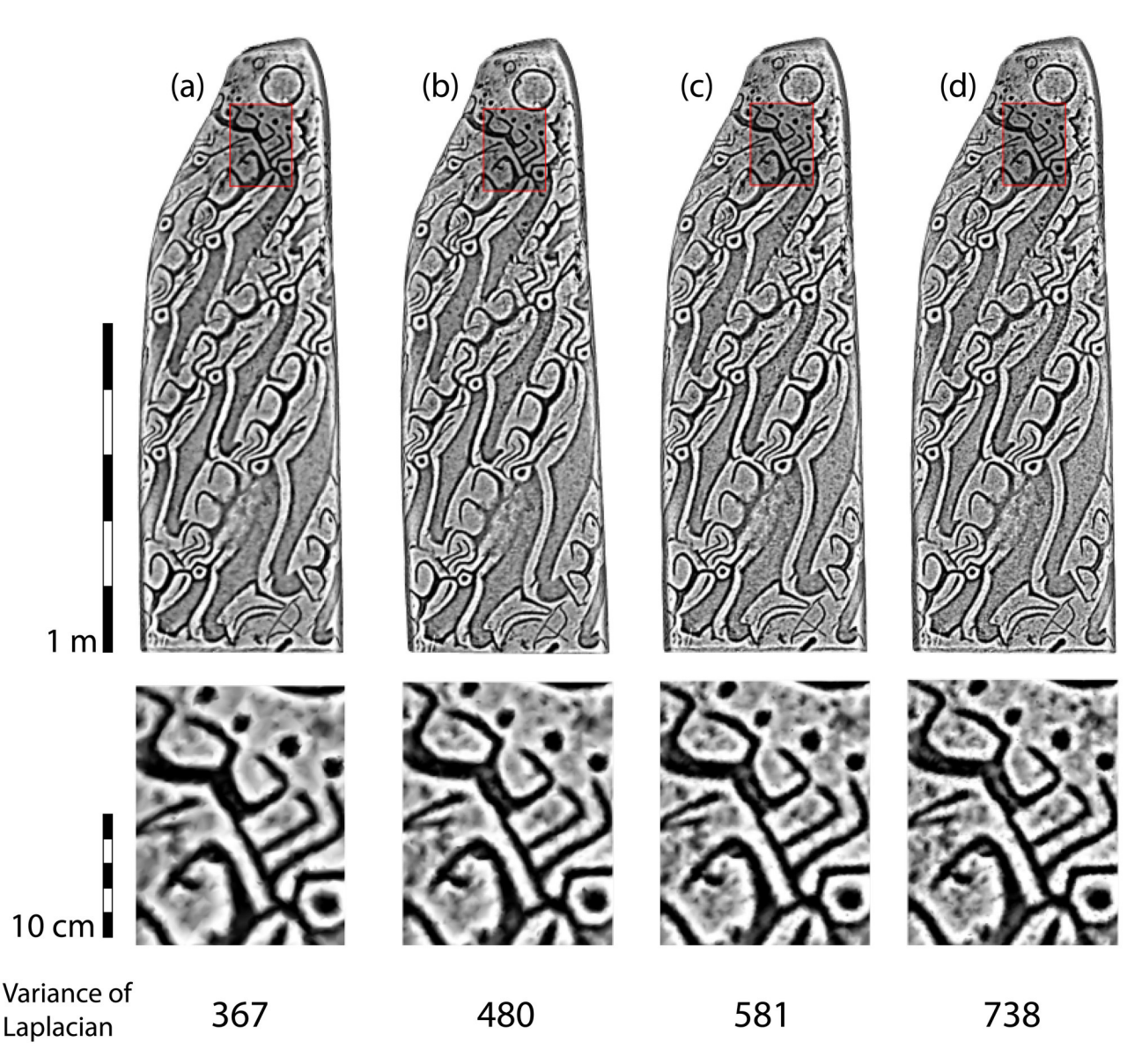
(a)
(b)
(c)
(d)
1 m
10 cm
Variance of Laplacian
367
480
581
738

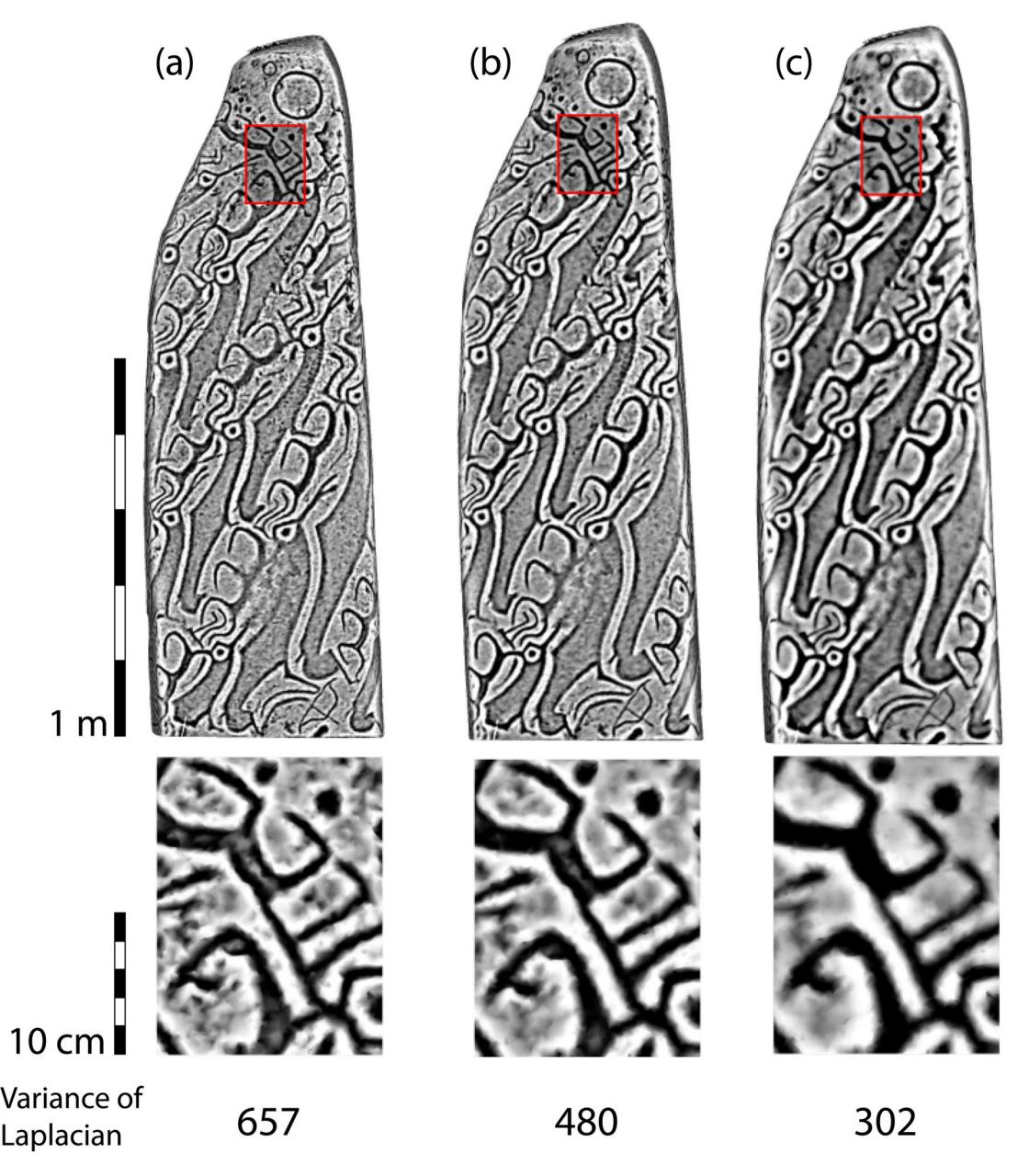
(a)
(b)
(c)
1 m
10 cm
Variance of Laplacian
657
480
302

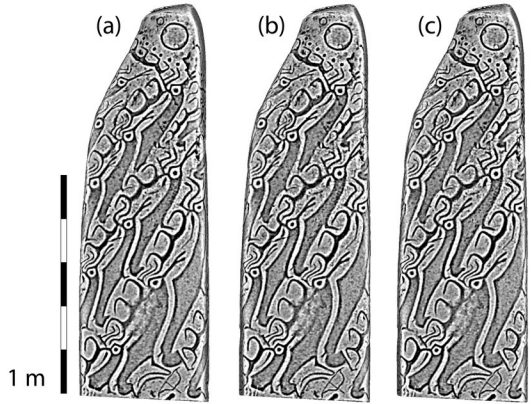
(a)
(b)
(c)
1 m

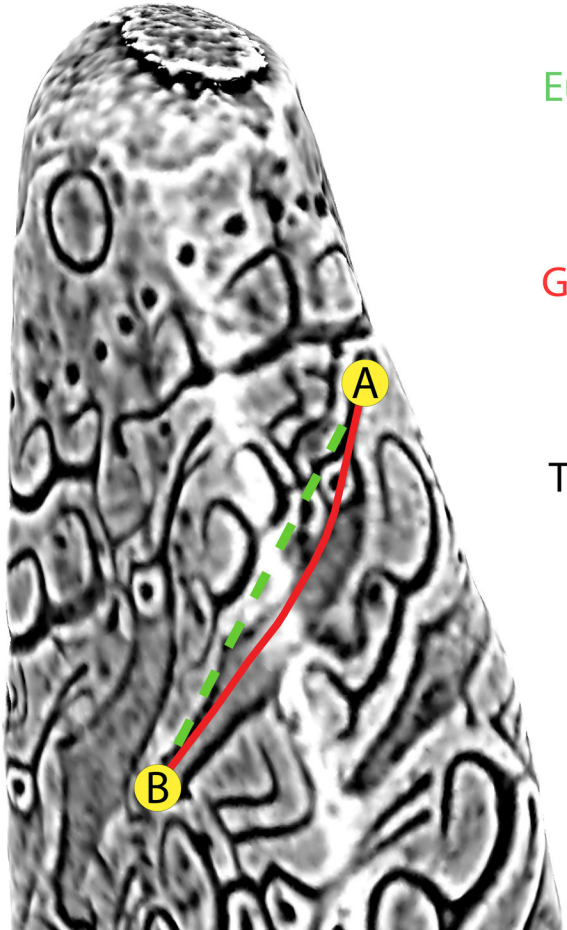

Euclidian distance AB : 33.8 cm

Geodesic distance AB : 38.1 cm

Total volume of stela : 0.287 m^3

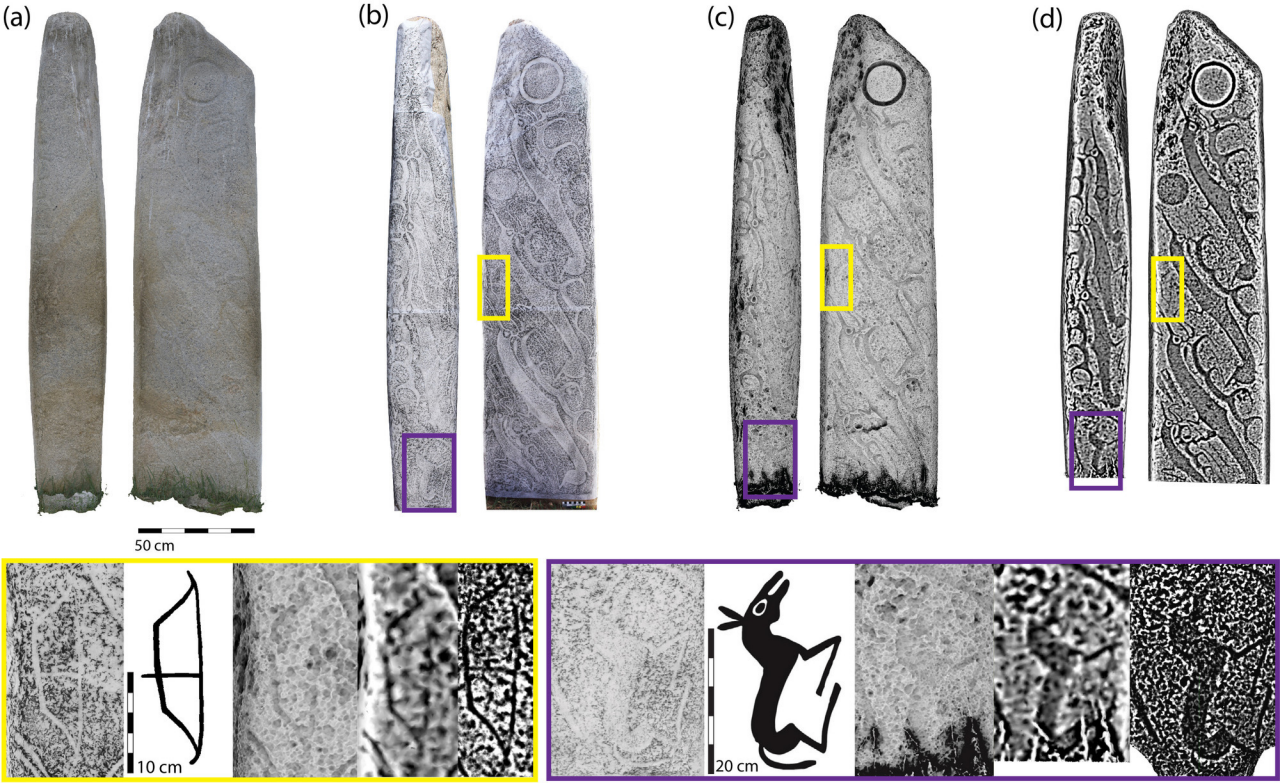
(a)
(b)
(c)
(d)
50 cm
10 cm
20 cm
(e)
(f)

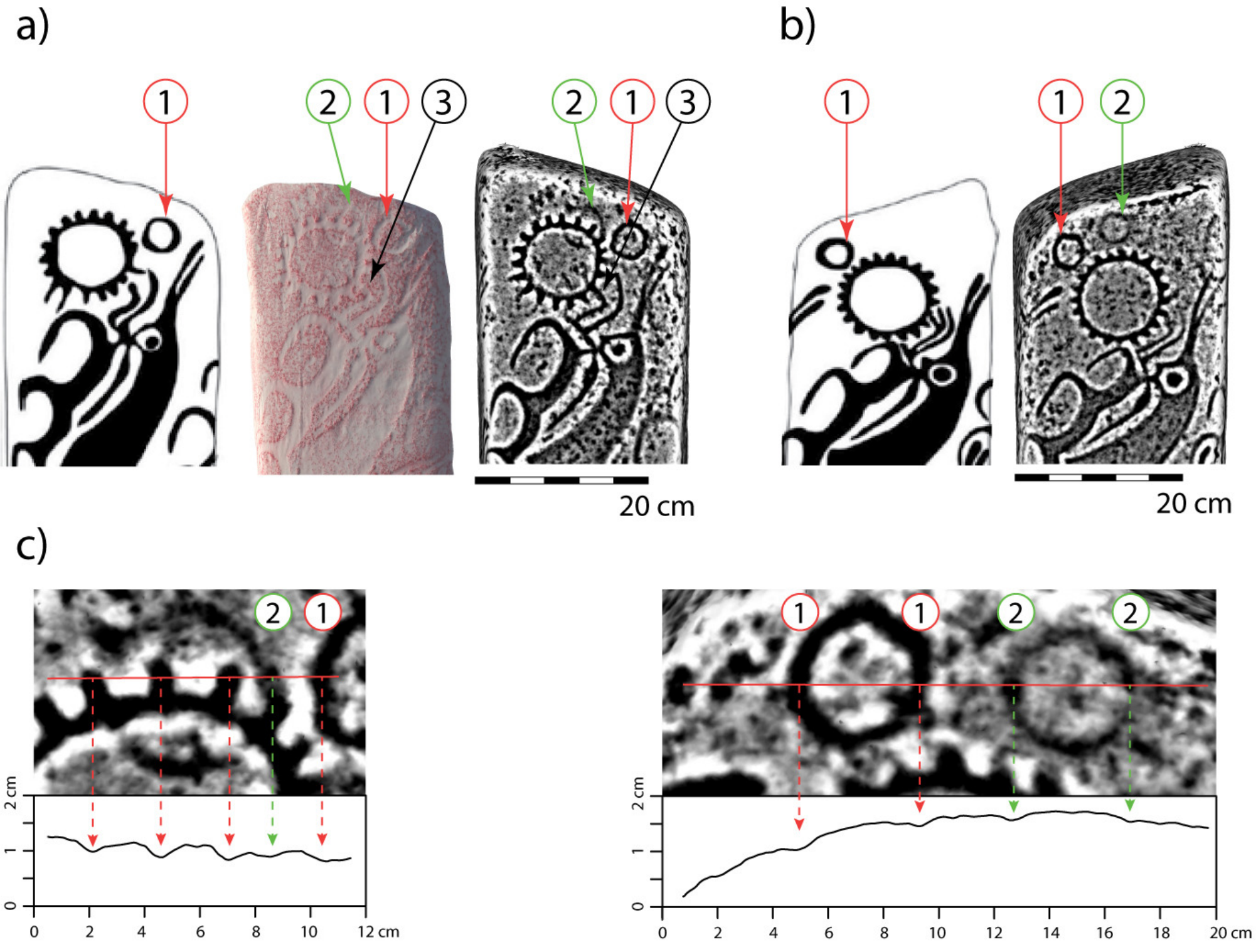
a)
1
2
1
3
2
1
3
20 cm
b)
1
1
2
20 cm
c)
2
1
2 cm
1
0
0
2
4
6
8
10
12 cm
1
1
2
2
2 cm
1
0
0
2
4
6
8
10
12
14
16
18
20 cm